Journal of Materials Chemistry C

ROYAL SOCIETY OF CHEMISTRY

PAPER

View Article Online
View Journal | View Issue

Cite this: J. Mater. Chem. C, 2025, 13, 23922

Structure–property coupling in lead-free halides $Rb_3Sb_2Br_9$ and $Rb_3Sb_2Br_6I_3$ obtained by mechanochemistry

Yousra Chakroun,[ab] Wajdi Cherif,[c] Brenda Martinelli,[d] Carlos A. López,[e] Javier Gainza,[f] Romualdo S. Silva Jr.,[a] Federico Serrano-Sánchez,[a] Mateus M. Ferrer,[e] C. Pecharromán,[a] João Elias F. S. Rodrigues *[f] and José A. Alonso *[a]

All-inorganic perovskites exhibit outstanding light absorption properties in the visible range, making them suitable for solar energy applications. We focus on the synthesis of $Rb_3Sb_2Br_9$ and $Rb_3Sb_2Br_6I_3$ halides using mechanochemical procedures. Synchrotron X-ray diffraction (SXRD) data were used for determining the crystallographic evolution in the temperature range 80–673 K. Two phases have been identified, the so-called 'low-temperature polymorph', with monoclinic symmetry (S.G: $P2_1/n$), and the 'high-temperature polymorph' with trigonal symmetry (S.G: $P\bar{3}m1$). At room temperature, SXRD data confirm the presence of a pure monoclinic phase for $Rb_3Sb_2Br_6I_3$ halide, whereas for $Rb_3Sb_2Br_9$, there is an admixture with the trigonal phase. The transition temperatures were estimated to be $T_t \sim 376$ K and ~390 K, for $Rb_3Sb_2Br_9$ and $Rb_3Sb_2Br_6I_3$, respectively, identified from the DSC curves. The monoclinic $P2_1/n$ structure is composed of double layers of irregular $[SbX_6]$ (X = Br, I) octahedra interconnected through common corners. Each octahedron shares three corners with adjacent octahedra, forming a two-dimensional network, with Rb ions located in the interlayer space. A more symmetric lattice is the trigonal $P\bar{3}m1$ polymorph, where the Sb atoms are coordinated in more regular $[SbX_6]$ polyhedra, also forming a 2D network. Symmetry-mode analysis reveals that monoclinic distortion is dominated by octahedral rotations, with cation translations and bond-length modulations acting as secondary stabilizing distortions. Infrared spectroscopy reveals a limited number of active optical phonons, with broader and red-shifted features in $Rb_3Sb_2Br_6I_3$, indicative of enhanced disorder compared to $Rb_3Sb_2Br_9$. The obtained values of the direct band gaps from UV-Vis-NIR spectroscopy measurements for the monoclinic phases are ~2.87 eV (for $Rb_3Sb_2Br_9$) and ~2.52 eV (for $Rb_3Sb_2Br_6I_3$). By correlating local distortions, electronic structure, and thermodynamic stability, our work establishes a microscopic view of phase competition in $Rb_3Sb_2X_9$ halides and provides design principles for environmentally benign, lead-free optoelectronic materials.

Received 25th August 2025,
Accepted 25th October 2025

DOI: 10.1039/d5tc03197d

rsc.li/materials-c

1. Introduction

The field of organic–inorganic lead halide perovskites has witnessed remarkable progress, with solar-cell efficiencies rapidly surpassing those of established semiconductor technologies, like CdTe and CIGS, within just a decade. The ability to fabricate perovskites through simple, low-cost solution-based processes positions them as a highly promising alternative to conventional photovoltaic technologies.[1–3] The paradigmatic example of hybrid organic–inorganic halide perovskites is $MAPbI_3$ (MA = methylammonium, $CH_3NH_3^+$), commonly known as MAPI.[4–6] However, its chemical instability under ambient conditions limits its practical applications.[7,8] Recent advances have been made across nearly every aspect of

[a] Instituto de Ciencia de Materiales de Madrid, CSIC, Cantoblanco, 28049 Madrid, Spain. E-mail: ja.alonso@icmm.csic.es
[b] Laboratory Inorganic Chemistry, Faculty of Sciences of Sfax, University of Sfax, 3000 Sfax, Tunisia
[c] National Engineering School of Sfax (ENIS), Laboratory of Electromechanical Systems (LASEM), B.P.W., 3038, Sfax, Tunisia
[d] CCAF, PPGCEM/CDTec, Federal University of Pelotas, 96010-610 Pelotas, Rio Grande do Sul, Brazil
[e] Instituto de Investigaciones en Tecnología Química (UNSL-CONICET) and Facultad de Química, Bioquímica y Farmacia, Almirante Brown 1455 (5700), San Luis, Argentina
[f] ESRF – European Synchrotron Radiation Facility, 38000 Grenoble, France. E-mail: rodrigues.joaoelias@gmail.com

perovskite solar cells (PSCs), revealing numerous properties of these hybrid materials. Compositional engineering strategies have been explored, including the development of all-inorganic and lead-free perovskites, along with an analysis of the associated challenges and opportunities. Beyond photovoltaics, recent research has been carried out into the use of perovskites in optoelectronic applications, such as X-ray detectors and image sensors, emphasizing their industrialization potential.

As mentioned, PSCs have rapidly advanced, achieving power conversion efficiencies of up to ~25% within a decade and showing strong potential to replace traditional silicon-based solar cells.[9,10] On the contrary, their practical application and commercialization are hindered by the toxicity of lead-based materials, which pose risks to human health and the environment. As a result, lead-free PSCs have emerged as a promising alternative, offering reduced toxicity, improved stability, and enhanced durability. Although lead-free perovskite solar-cells have reached power conversion efficiencies of ~15%, further development is needed to close the performance gap.[11–14] Certainly, the choice of cations and anions influences both the efficiency and stability of these materials. Nevertheless, designing environmentally friendly lead-free perovskite devices remains a critical goal, and exploring alternative compositions and structures is well worth pursuing.

Over the past years, considerable efforts have been made to identify novel lead-free alternatives, including various perovskite and perovskite-like materials. While tin (Sn) and germanium (Ge) – elements in the same group as Pb – have been considered, their tendency to oxidize from the +2 to the +4 state undermines their stability. In contrast, bismuth (Bi) and antimony (Sb), which form stable +3 ions with electronic configurations like Pb^{2+}, present more viable options. Sb-based perovskite-like compounds have demonstrated improved stability and competitive photovoltaic performance.[15] Rubidium antimony halides[16–18] have emerged as a promising low-toxicity alternative to organo-lead halide perovskites for photovoltaic applications. The effect of the bromide-to-iodide ratio in $Rb_3Sb_2Br_{9-x}I_x$ (x = 0–9) compositions on the structural, optical, and photovoltaic properties has been examined.[16] In this system, all the compositions have been described as a 2D-layered monoclinic crystal structure. Although replacing iodide with the smaller bromide ion does not alter the crystal system, increasing the bromide content reduces the unit-cell size and induces a blue shift in the absorption edge, widening the band gap from 2.02 up to 2.46 eV. Moreover, solar cells utilizing $Rb_3Sb_2I_9$ as the absorber achieve a power conversion efficiency of 1.37%.[16] Although these compounds exhibit relatively wide band gaps, such characteristics are advantageous for their potential use in tandem solar cells,[19,20] where high bandgap materials serve as top absorbers to harvest the high-energy portion of the solar spectrum. In this configuration, they complement lower bandgap materials, contributing to improved overall device efficiency.

Mechanochemical synthesis has emerged as a sustainable route for preparing halide perovskites. Unlike conventional solution-based methods, mechanochemistry allows the solvent-free formation of crystalline phases under ambient conditions, minimizing waste and avoiding solvent-related contamination.[21–26] This approach also enables precise control of stoichiometry, high reproducibility, and rapid reaction kinetics, which are particularly advantageous for the synthesis of air- and moisture-sensitive halide systems. Moreover, the mechanical activation often promotes metastable phase formation and enhanced homogeneity at the atomic level, providing an efficient and environmentally friendly alternative for the preparation of complex halide perovskites.

Recent years have seen extensive research on $A_3B_2X_9$ halide perovskites (A = Cs, Rb; B = Sb, Bi; X = Cl, Br, I), focusing on their synthesis, structural diversity, and optoelectronic properties. Several studies have reported on $Rb_3B_2X_9$ compounds, revealing their potential for optoelectronic and energy-related applications.[27–30] Despite these advances, a detailed understanding of the structural phase transitions and their correlation with local distortions and electronic behavior remains limited. In this work, we address this gap by combining temperature-dependent X-ray and distortion-mode analysis with optical and theoretical results, providing a unified picture of the structural and electronic evolution in $Rb_3Bi_2Br_9$ and $Rb_3Bi_2Br_6I_3$. We report on the synthesis process of lead-free, environmentally friendly rubidium antimony bromide-iodine, prepared using a sustainable mechanochemical synthesis method with green credentials. Temperature-dependent synchrotron X-ray diffraction (SXRD) was employed to investigate their crystal structures and structural phase transitions. A more detailed interpretation of the phase transition was achieved through distortion-mode analysis,[31–33] which enabled rigorous identification and quantification of the symmetry-adapted distortions responsible for the lowering from trigonal to monoclinic symmetry in $Rb_3Sb_2Br_9$. This approach provides a microscopic picture of the structural instabilities driving the transition. Optical characterization reveals strong UV-Vis-NIR absorption and photoluminescence centered around 400 nm, underscoring their potential for a broad range of applications.

2. Experimental methods

2.1. Synthesis

$Rb_3Sb_2Br_9$ and $Rb_3Sb_2Br_6I_3$ polycrystalline powders were synthesized *via* a mechanochemical approach using a planetary ball mill. Stoichiometric amounts of $SbBr_3$, RbBr, and RbI (total mass: 1 g) were mixed and placed into a zirconia-lined jar with 20 zirconia balls (5 mm in diameter) inside a nitrogen-filled glovebox. The sealed jar was subjected to ball milling for 3 h at 450 rpm under an inert N_2 atmosphere using a Retsch PM100 mill.

2.2. Structural characterization

Room-temperature powder X-ray diffraction (XRD) data were collected using a Bruker D5 diffractometer with Cu-$K\alpha$ radiation (λ = 1.5418 Å). To investigate the structural evolution with temperature, synchrotron X-ray diffraction (SXRD) patterns

were collected in the range of 80–673 K at the beamline ID22[34] of the European Synchrotron Radiation Facility (Grenoble, France), using a wavelength of 0.35434 Å (~35 keV). The samples were loaded into 0.5 mm quartz capillaries and continuously rotated during acquisition. A LN_2-based cryostream was used to cool down the sample, while a hot air blower was employed to heat up the samples above 295 K. Rietveld refinements from SXRD data were conducted using *FullProf Suite*.[35] The refined parameters included: zero-point error, background coefficients, scale factor, peak asymmetry, lattice constants, atomic fractional coordinates (x,y,z), and isotropic thermal displacement parameters (U_{iso}).

2.3. Thermal and morphological characterization

Differential scanning calorimetry (DSC) measurements were carried out using a Mettler TA3000 system over the temperature range 120–650 K, with heating and cooling rates of 10 K min^{-1} and using ~70 mg of sample (see in Fig. S1). Elemental composition was assessed by energy dispersive X-ray spectroscopy (EDXS), performed at an acceleration voltage of 18 kV and an acquisition time of 60 s (see in Fig. S2 and S3). Morphological analysis was performed using field emission scanning electron microscopy (FE-SEM) on a FEI Nova microscope operating at 5 kV.

2.4. Optical and infrared properties

Optical properties were evaluated by diffuse reflectance UV-Vis-NIR spectroscopy using a Jasco 660 V spectrophotometer attached with an integrating sphere. The absorbance of $Rb_3Sb_2Br_9$ and $Rb_3Sb_2Br_6I_3$ was analyzed using the Kubelka–Munk function, where the optical absorption coefficient [$\alpha(\nu)$] was calculated *via* the relation $F(\nu; R) \propto \alpha(\nu) = (1-R)^2/2R$, being R the angular integrated diffuse reflectance as a function of photon energy ($h\nu$). Far infrared spectra were taken by a FTIR spectrophotometer Bruker Vertex 70 V, using an extended spectral range beam splitter, a globar source, and a DTGS detector (seeFig. S4). Dense pellets were prepared by cold pressure sintering using an optically polished zirconia die. The solid pellets were measured by a near-normal reflectance attachment.

2.5. Density functional theory

Density functional theory (DFT) calculations were carried out using the *CRYSTAL23* simulation package[36] with the *HSE06* hybrid functional.[37] Triple-zeta-valence basis sets with polarization (POB-TZVP), as developed by Laun and co-workers, were employed for rubidium (Rb), antimony (Sb), and bromine (Br) atomic centers[38] in the $Rb_3Sb_2Br_9$ halide. The convergence of the infinite Coulomb and Hartree–Fock (HF) exchange series was controlled through five accuracy parameters (α_k, k = 1–5): α_1 for overlap, α_2 for Coulomb integral penetration, α_3 for HF exchange overlap, and α_4/α_5 for pseudo-overlaps in the HF-exchange series. The chosen values were 8, 8, 8, 8, and 16, respectively. Brillouin zone sampling was performed with a Pack–Monkhorst grid, using shrinking factors of 8 × 8, in combination with the Gilat net method for integration.

3. Results

3.1. Initial characterization

$Rb_3Sb_2Br_9$ (hereafter labelled as Br9) and $Rb_3Sb_2Br_6I_3$ (hereafter labelled as Br6I3) were obtained as pale yellow or orange microcrystalline powders, respectively. The initial identification of the samples was carried out from laboratory X-ray diffractometry at room temperature, as illustrated in the Le Bail fits of Fig. 1. The diffraction patterns are in agreement with the monoclinic crystal structures reported more than twenty years ago by Abrahams *et al.* from single-crystal laboratory X-ray diffraction.[39]

Field emission scanning electron microscopy (FE-SEM) images presented in Fig. 2 provide detailed insight into the microstructure of the materials, synthesized *via* ball milling. For $Rb_3Sb_2Br_6I_3$, at low magnification (23 545×, Fig. 2a), one can observe that the sample consists of clusters of irregularly shaped particles of varying sizes, in the micrometric range. Higher magnifications (26 870× and 50 000 ×, Fig. 2b and c) reveal further details: these clusters consist of compact

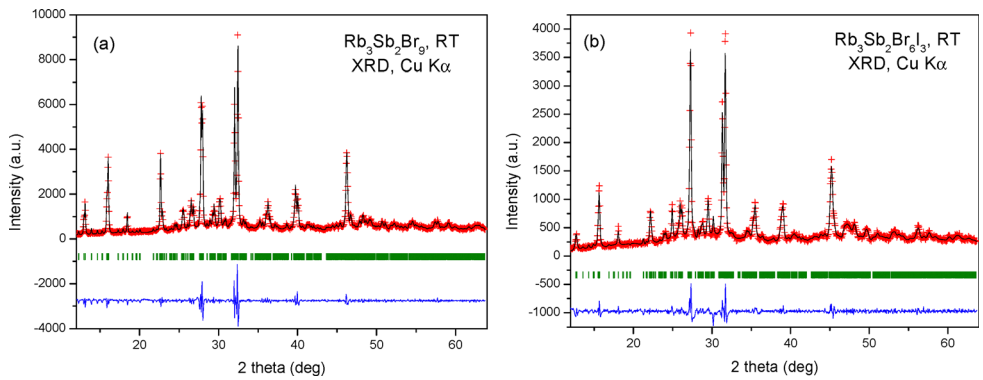

Fig. 1 Le Bail fits for the mechanochemically prepared (a) $Rb_3Sb_2Br_9$ and (b) $Rb_3Sb_2Br_6I_3$ at room temperature from laboratory XRD data from Cu-$K\alpha$ radiation. Le Bail plot: observed (red cross) and calculated (black line) X-ray diffraction pattern. Blue lines represent the fit residuals, and the green bars are the expected Bragg reflections.

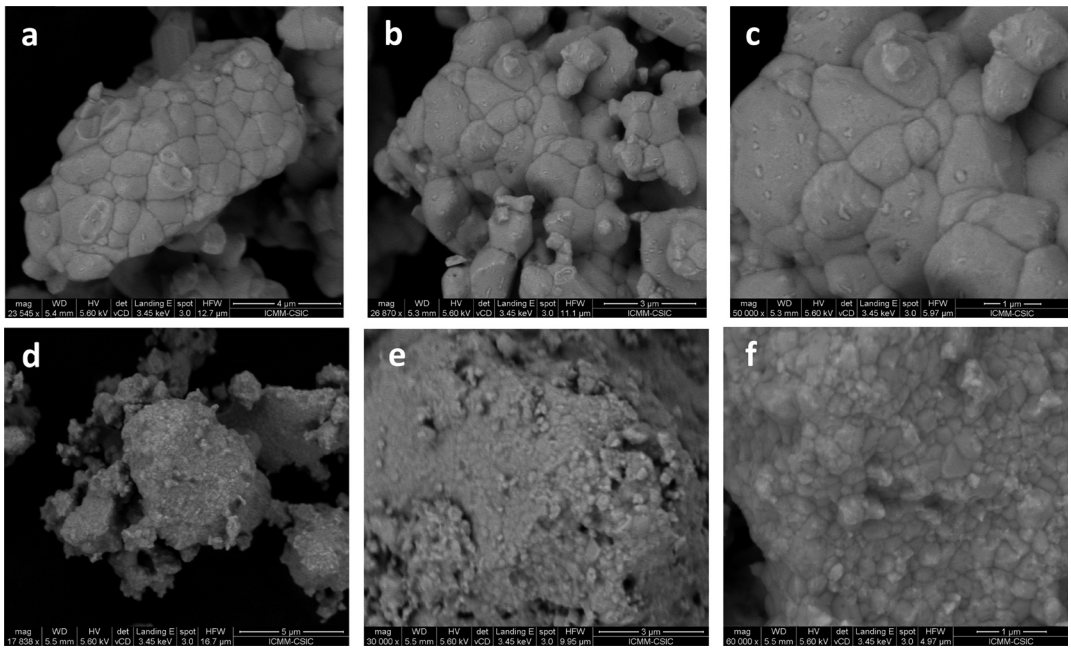

Fig. 2 FE-SEM images for (a)–(c) $Rb_3Sb_2Br_6I_3$ and (d)–(f) $Rb_3Sb_2Br_9$, with magnifications of 23 545× (a), 26 870× (b), 50 000× (c), 17 838× (d), 30 000× (e), and 60 000× (f).

microparticles with well-defined, sharp edges, typically ranging in size from ~0.5 to 1 μm, with some of them overpassing one micron. For $Rb_3Sb_2Br_9$, the phenomenology is quite similar, although in this case the agglomerates (see Fig. 2d–f) consist of microparticles of smaller size, in the 0.2–0.5 μm range (see Fig. 2f). It is noteworthy that these well-shaped and well-crystallized particles are formed during the ball-milling process, in connection with the crystallinity observed in the SXRD patterns. Energy-dispersive X-ray spectroscopy (EDXS), conducted alongside the FE-SEM analysis, indicates an approximate atomic ratio of 3:2:6:3 for Rb:Sb:Br:I ratios. This atomic ratio confirms the stoichiometry obtained by diffraction methods. A representative EDX spectrum is shown in Fig. S3.

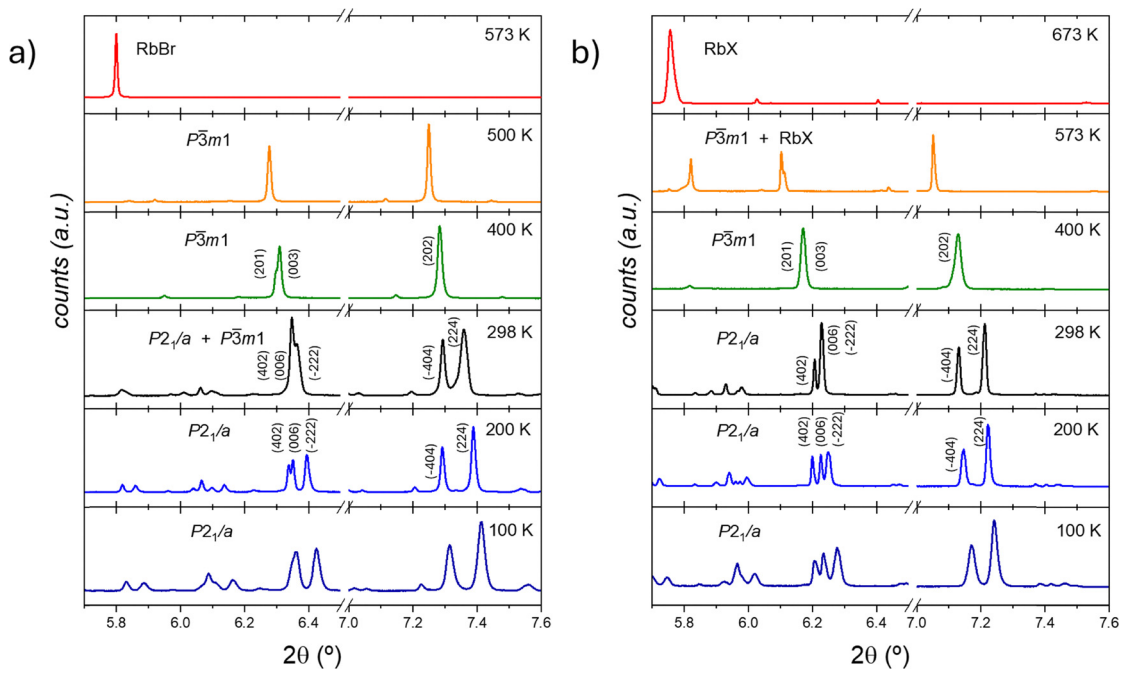

Fig. 3 Thermal evolution of the raw synchrotron X-ray diffractions patterns for (a) $Rb_3Sb_2Br_9$ and (b) $Rb_3Sb_2Br_6I_3$ phases at selected 2θ angular interval 5.8–7.6°. Miller indices (*hkl*) are highlighted in the SXRD patterns of both monoclinic and trigonal phases.

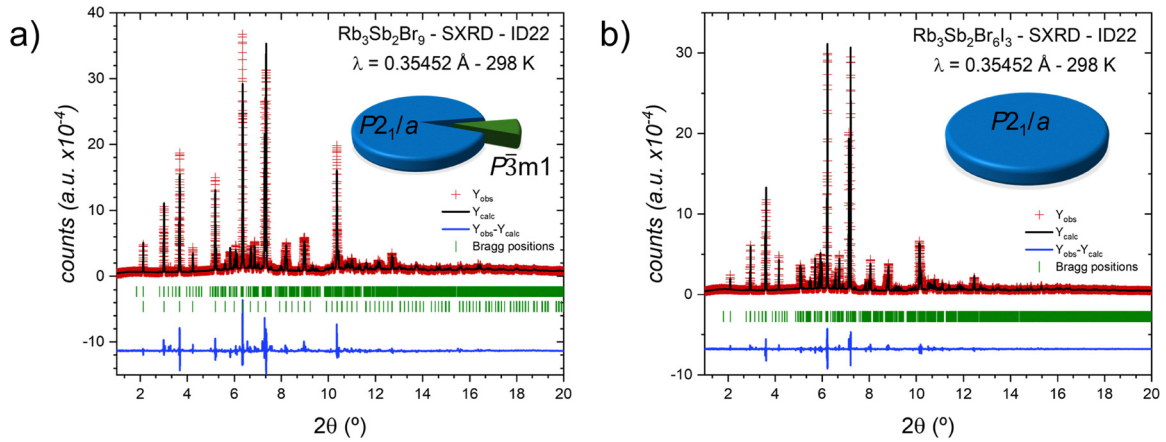

Fig. 4 Rietveld refinement of SXRD patterns, collected at room temperature with (a) x = 0 and (b) x = 3. Inset charts indicate the phase distribution of both monoclinic and trigonal phases. Rietveld plot: observed (red cross) and calculated (black line) synchrotron X-ray diffraction pattern. Blue lines represent the fit residuals, and the green bars are the expected Bragg reflections.

3.2. Structural analysis from SXRD data

A detailed structural investigation of $Rb_3Sb_2Br_9$ and $Rb_3Sb_2Br_6I_3$, including their thermal evolution, was carried out using SXRD data collected at selected temperatures: 80, 100, 200, 298, 400, 500, 573, and 673 K. A comparative analysis of the diffraction patterns of both phases at different temperatures reveals a phase transition between 300 and 400 K, which matches with the monoclinic symmetry (S.G: $P2_1/n$) and the trigonal symmetry (S.G: $P\bar{3}m1$), respectively. The high-temperature polymorph observed at 573 K exhibits signals of the rubidium halide. At 673 K, only the RbBr (or RbX for mixed halide perovskite) is identified in both diffractograms, demonstrating that these phases decompose between 573 and 673 K. In fact, the thermogravimetry analysis unveiled decomposition temperatures of ~608 and ~585 K for $Rb_3Sb_2Br_9$ and $Rb_3Sb_2Br_6I_3$, respectively (see Fig. S1). Additionally, it is possible to notice that the undoped phase (Br9) signals of a mixture of both polymorphs at room temperature. The thermal evolution of selected diffraction lines from 100 up to 673 K is plotted in Fig. 3.

The preliminary Rietveld refinement at room temperature confirms the presence of the monoclinic symmetry (S.G: $P2_1/n$) and, only for $Rb_3Sb_2Br_9$, the additional coexistent trigonal phase (S.G: $P\bar{3}m1$), as is exhibited in Fig. 4.

In the $P2_1/n$ structure (non-standard setting), all Rb^+, Sb^{3+}, and Br^- ions are located at the 4e (x, y, z) Wyckoff sites, with three distinct rubidium, two antimuonium, and nine bromine sites. The crystal structure is composed of layers of [$SbBr_6$] octahedra interconnected through corner-sharing. Each octahedron shares three of its vertices with adjacent octahedra, forming a two-dimensional network. The three remaining bromine atoms, located on the opposite face of each octahedron, extend outward and coordinate with rubidium cations situated in the interlayer spaces. A more symmetric lattice is obtained in the $P\bar{3}m1$ space-group, where the Sb atoms occupy the 2d ($^1/_3$, $^2/_3$, z) Wyckoff site, while the bromides are distributed in both 3e ($^1/_2$, 0, 0) and 6i (x, -x, z) positions, levelled Br1 and Br2, respectively. The rubidium cations are also distributed in two sites: 1a (0, 0, 0) and 2d ($^1/_3$, $^2/_3$, z), named Rb1 and Rb2, respectively. The schematic views of both symmetries for $Rb_3Sb_2Br_9$ at room temperature are presented in Fig. 5. The main crystallographic data at room temperature for $Rb_3Sb_2Br_9$ are listed in Table 1. The high-temperature crystallographic data at 400, 500, and 573 K are summarized in Tables S1–S3 for $Rb_3Sb_2Br_9$, respectively.

As previously discussed, the monoclinic model features the bromine atoms occupying nine distinct crystallographic sites. Consequently, in the iodine-doped phase, there exist many possible configurations for accommodating six bromine and

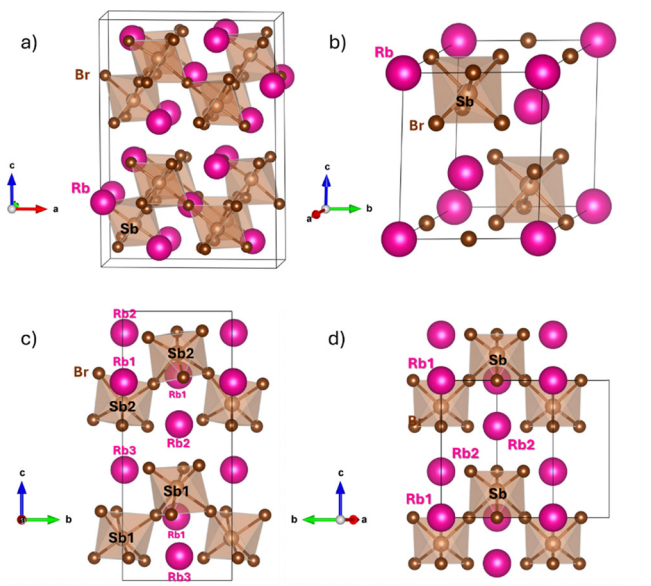

Fig. 5 Schematic view of the monoclinic (a) and (c) and trigonal (b) and (d) $Rb_3Bi_2Br_9$ crystal structures. Panels (c) and (d) illustrate equivalent views of the monoclinic and trigonal phases, where the octahedral tilting can be noticed. Pink, light brown, and dark brown spheres represent Rb, Sb, and Br atoms.

Table 1 Crystallographic data for $Rb_3Sb_2Br_9$ halide from SXRD data at 298 K, defined in the monoclinic $P2_1/n$ space-group (non-standard setting), Z = 4. a = 13.6616(3) Å, b = 7.81826(9) Å, c = 19.2733(4) Å, β = 90.378(1)°, and V = 2058.54(7) Å^3

Atom	x	y	z	U_{iso} (Å^2)	f_{occ}
Rb1	0.0063 (13)	−0.0023 (16)	0.2597 (8)	0.150 (3)	1
Rb2	−0.3282 (8)	0.0132 (11)	0.9194 (5)	0.074 (3)	1
Rb3	−0.3424 (10)	0.0280 (11)	0.4083 (6)	0.119 (4)	1
Sb1	−0.3345 (5)	−0.0035 (10)	0.1576 (3)	0.050 (2)	1
Sb2	−0.3357 (5)	−0.0031 (9)	0.6564 (3)	0.043 (2)	1
Br1	−0.0056 (12)	−0.5574 (8)	0.2472 (7)	0.085 (3)	1
Br2	−0.3230 (9)	−0.5027 (11)	0.9242 (5)	0.077 (3)	1
Br3	−0.3296 (9)	−0.4507 (9)	0.4184 (6)	0.079 (4)	1
Br4	−0.0889 (8)	−0.2670 (13)	0.9284 (6)	0.073 (4)	1
Br5	−0.0559 (8)	−0.2956 (13)	0.4204 (6)	0.066 (4)	1
Br6	−0.4099 (7)	−0.2765 (13)	0.5940 (6)	0.067 (4)	1
Br7	−0.3937 (10)	−0.2530 (18)	0.0814 (8)	0.123 (6)	1
Br8	−0.7551 (9)	−0.2763 (15)	0.2706 (7)	0.101 (5)	1
Br9	−0.7200 (7)	−0.3037 (12)	0.7617 (6)	0.075 (4)	1

R_p = 5.96%, R_{wp} = 6.94%, R_{exp} = 1.52%, χ^2 = 20.9, R_{Bragg} = 13.1%. Secondary phase: space group: $P\bar{3}m1$, a = 7.8563(3) Å, c = 9.6430(7) Å, and V = 515.44(5) Å^3. Amount: 8.1(1)% w/w

three iodine atoms within the structure. Due to the coupling of refinement parameters, it is not feasible to independently determine the Br/I ratio at each individual site. To solve this issue, firstly, we refine the bromine/iodine distribution in the more symmetrical polymorph (at 400 K), where the iodine atoms are distributed on just two sites (3e and 6i). In this case, it was possible to obtain the Br/I occupancy and confirm experimentally that the Br/I ratio is close to 6/3, or in other words $x \approx 3$. After confirming that the Br/I ratio agrees with the expected, the refinements at room were revised considering a free distribution of Br and I in the nine sites, but with a linear restraint, which fixes the x in 3. The main crystallographic data at room temperature for $Rb_3Sb_2Br_6I_3$ is listed in Table 2. Tables S4–S6 summarize the high-temperature crystallographic data at 400, 500, and 573 K for $Rb_3Sb_2Br_6I_3$, respectively.

The thermal evolutions of crystal structures were evaluated from different perspectives, as discussed next. The unit-cell volume normalized per formula unit (Z) is plotted in Fig. 6a. As expected, the iodine-doped phase exhibits an increase in the volume of ~6%. In both phases, the volume expands linearly with temperature, and no abrupt changes are observed across the structural phase transitions. However, the thermal evolution of the unit cell along individual crystallographic directions presents subtle differences, emerging during the phase transitions. The temperature-dependence of the a, b, and c unit-cell parameters for the monoclinic phase ($P2_1/n$), as well as the corresponding values for the $P\bar{3}m1$ symmetry, are plotted in Fig. 6b–d. These plots reveal that the low-temperature phase distortion leads to an elongation along the a-axis and a contraction along the b-axis. The c-axis remains largely unaffected by the phase transition. From the perspective of the layered structure, this behavior suggests that the [SbX_6] layers expand along the a-direction and contract along the b-direction upon transitioning to the low-temperature phase, while the interlayer spacing remains almost invariant.

Table 2 Crystallographic data for $Rb_3Sb_2Br_6I_3$ halide from SXRD data at 298 K, defined in the monoclinic $P2_1/n$ space-group (non-standard setting), Z = 4. a = 13.9862(1) Å, b = 7.98342(7) Å, c = 19.6496(2) Å, β = 90.4542(2)°, and V = 2193.96(3) Å^3

Atom	x	y	z	U_{iso} (Å^2)	f_{occ}
Rb1	0.0130 (5)	−0.0185 (10)	0.2642 (3)	0.104 (2)	1
Rb2	−0.3284 (4)	0.0132 (9)	0.9160 (3)	0.116 (3)	1
Rb3	−0.3397 (5)	0.0128 (11)	0.4032 (3)	0.112 (3)	1
Sb1	−0.3339 (3)	0.0055 (6)	0.1585 (2)	0.033 (1)	1
Sb2	−0.3355 (3)	−0.0006 (7)	0.6573 (2)	0.039 (1)	1
Br1/I1	−0.0019 (7)	−0.5571 (6)	0.2496 (4)	0.100 (3)	0.81/0.19 (1)
Br2/I2	−0.3275 (4)	−0.5588 (7)	0.9201 (3)	0.116 (4)	0.55/0.45 (2)
Br3/I3	−0.3277 (3)	−0.4714 (6)	0.4197 (2)	0.061 (2)	0.53/0.47 (2)
Br4/I4	−0.0872 (4)	−0.2808 (7)	0.9347 (3)	0.072 (3)	0.54/0.46 (2)
Br5/I5	−0.0548 (4)	−0.2867 (7)	0.4198 (3)	0.076 (3)	0.59/0.41 (2)
Br6/I6	−0.4124 (4)	−0.2862 (7)	0.6001 (3)	0.085 (3)	0.58/0.42 (2)
Br7/I7	−0.3936 (4)	−0.2656 (7)	0.0882 (3)	0.105 (3)	0.51/0.49 (3)
Br8/I8	−0.7550 (5)	−0.2919 (8)	0.2732 (3)	0.060 (2)	1.00/0.00 (3)
Br9/I9	−0.7130 (4)	−0.3050 (7)	0.7574 (3)	0.061 (2)	0.88/0.12 (2)

R_p = 3.81%, R_{wp} = 4.44%, R_{exp} = 1.86%, χ^2 = 5.7, R_{Bragg} = 7.19%

3.3. Diffuse reflectance

By measuring the diffuse reflectance at room conditions, we have obtained the Kubelka–Munk function, which is nearly proportional to the absorption coefficient [$\alpha(\nu)$]. To derive an approximate value of the bandgap, we have employed the Tauc-plot method. The function $[F(R)\cdot E]^2$ has been plotted *versus* energy, as exhibited in Fig. 7a. According to the Tauc approximation, the crossing of the fitting of the rise of this function with the x-axis determines the energy of the direct optical bandgap. The obtained values of the direct bandgap for both monoclinic phases $Rb_3Sb_2Br_9$ and $Rb_3Sb_2Br_6I_3$ are ~2.87 eV and ~2.52 eV,[40] respectively.

Theoretical band structure calculations for $Rb_3Sb_2Br_9$ reveal a direct band gap of ~2.65 eV along the Γ–Γ path in the first Brillouin zone (see Fig. 7c). Although this value is slightly lower than the experimentally determined one (~2.87 eV), the agreement can be considered satisfactory when accounting for the low symmetry of the space-group and the intrinsic limitations associated with the choice of exchange–correlation functionals. The projected density of states in Fig. 7b indicates that the valence band is primarily composed of Br and Sb orbitals, with comparable contributions from both species. In contrast, the conduction band is dominated by Br orbitals, while Sb states contribute to a lesser extent to the electronic transition processes. This predominance of Br orbitals in the conduction region can be attributed to their higher electronegativity, which facilitates photon absorption and enhances excitation probability.

3.4. Infrared optical phonons

We measured the infrared response of both compounds using near-normal reflectance [$R(\nu)$] on pressure-sintered pellets over the spectral range 40–4000 cm^{-1} at room conditions (see Fig. S4). The dominant high-frequency vibrational mode was observed at ~200 cm^{-1}. To estimate the most intense phonon frequencies, we applied Kramers–Krönig (KK) transformations to the logarithm of the reflectance spectrum to obtain the

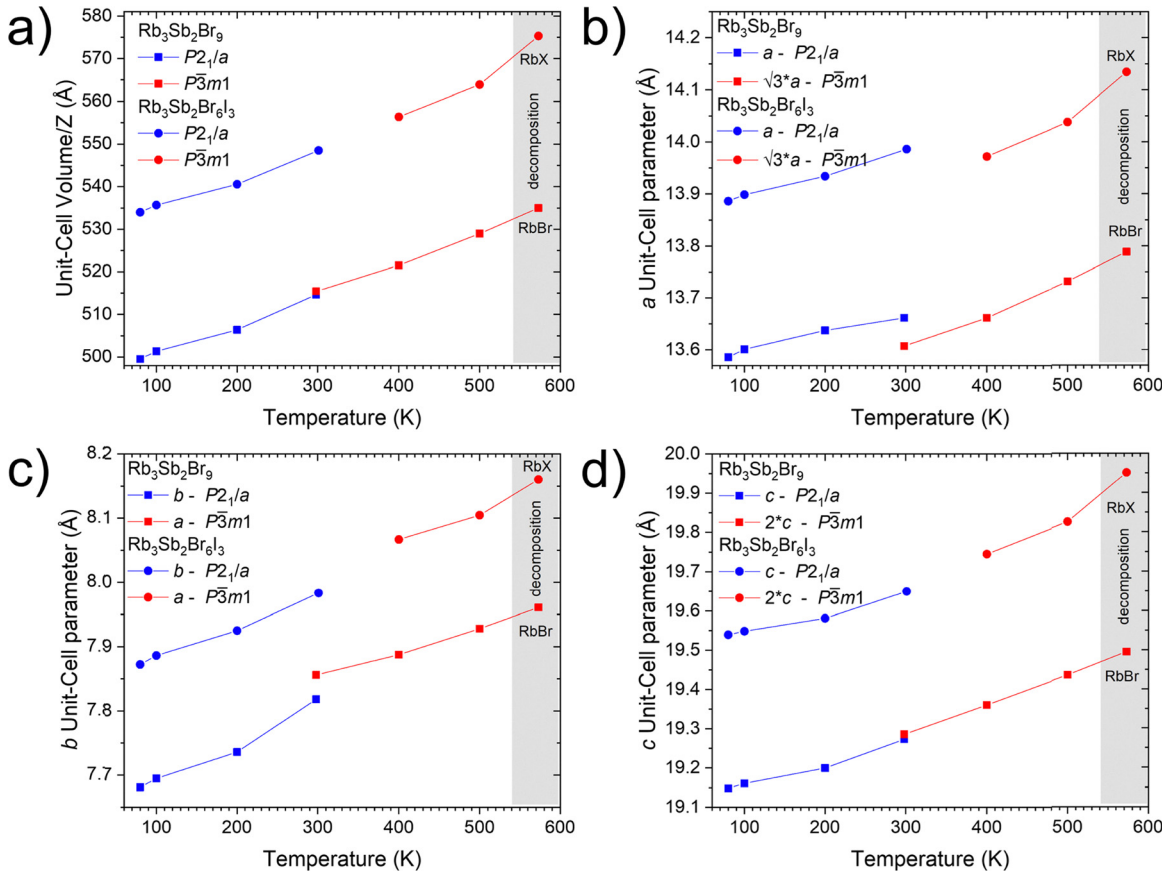

Fig. 6 Thermal evolution of refined unit-cell parameters: (a) unit-cell volume/*Z*, (b) *a*, (c) *b*, and (d) *c* lattice parameters for both $Rb_3Sb_2Br_9$ and $Rb_3Sb_2Br_6I_3$ halides. The gray region above 573 K denotes the onset of decomposition for both samples, in good agreement with the thermogravimetric analysis shown in Fig. S1.

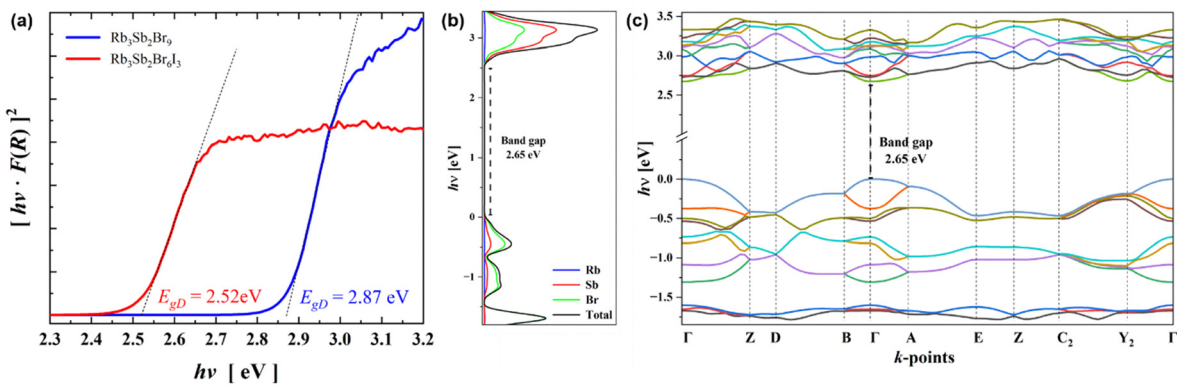

Fig. 7 Tauc-plot of monoclinic $Rb_3Sb_2Br_9$ and $Rb_3Sb_2Br_6I_3$ halide compounds (a). Electronic properties of $Rb_3Sb_2Br_9$ from DFT calculations: projected density of states (b) and electronic band structure (c) with a direct gap of 2.65 eV at Γ–Γ.

phase and subsequently to determine the real and imaginary components of the effective dielectric function $[\varepsilon(\nu)]$ of the pellets. The real part and imaginary parts of $\varepsilon(\nu)$ extracted from the reflectivity spectrum by KK analysis are plotted in Fig. 8.

Synchrotron X-ray diffraction results confirmed that both compounds adopt monoclinic symmetry, for which standard group-theoretical analysis[41,42] predicts 81 infrared-active modes ($\Gamma_{IR} = 41A_u \oplus 40B_u$), in contrast to only 14 infrared-active modes for the trigonal phase ($\Gamma_{IR} = 6A_{2u} \oplus 8E_u$). Experimentally, however, only eight modes are visible in $Rb_3Sb_2Br_9$ (three intense) and four in $Rb_3Sb_2Br_6I_3$. It should be noticed that infrared measurements were carried out on pressed powder pellets; then the recorded spectra represent angular averages of the three components of the refractive

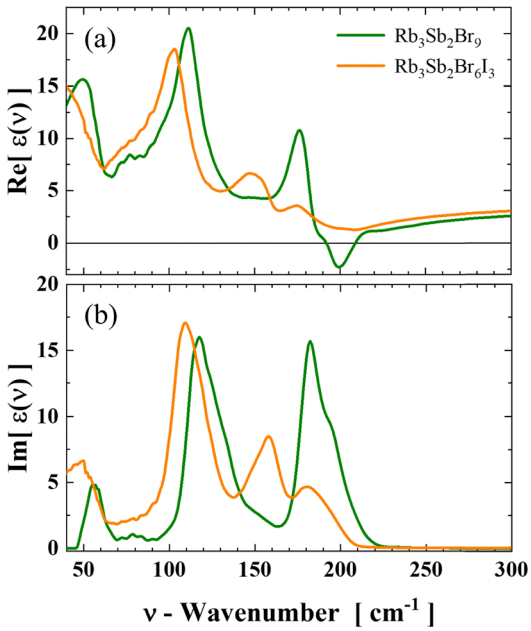

Fig. 8 Real (a) and imaginary (b) parts of the effective dielectric function [$\varepsilon(\nu)$] of $Rb_3Sb_2Br_9$ and $Rb_3Sb_2Br_6I_3$ halides in the far- and mid-infrared regions.

index tensor ($n_{\mu\nu}$) in the monoclinic structure. The reduced number of resolved modes likely indicates that many of them cluster within very narrow frequency windows, making individual contributions indistinguishable (*i.e.*, almost accidental degeneracy).

For $Rb_3Sb_2Br_9$, this angular averaging effect may mimic the response of the trigonal phase, as the number of observed modes is close to the theoretical prediction for that structure. In contrast, $Rb_3Sb_2Br_6I_3$ exhibits broader and slightly red-shifted bands compared to $Rb_3Sb_2Br_9$, as evidenced in the imaginary part of the effective dielectric function (see Fig. 8). The red shift can be attributed to the mass difference between Br^- and I^- anions, while the broadening suggests a higher degree of disorder. Furthermore, the three high-frequency bands observed in $Rb_3Sb_2Br_9$ (a weak feature at 151 cm^{-1} and a strong doublet at 182 and 195 cm^{-1}) display a different intensity distribution in $Rb_3Sb_2Br_6I_3$, where a strong band appears at 159 cm^{-1} and a weaker single band at 182 cm^{-1}. This rearrangement points to local atomic ordering of I^- anions, forming nanometer-scale regions with partial order but substantial broadening due to limited crystallite size. Finally, the transverse (ν_{TO}) and longitudinal (ν_{LO}) optical frequencies were determined from the maximum of the imaginary part and the minimum of the absolute value of the effective dielectric function, respectively, as listed in Table 3. Theoretical description of this optical phonons determination can be found elsewhere.[43–45]

Table 3 List of the transverse (ν_{TO}) and longitudinal (ν_{LO}) optical frequencies estimated from the effective dielectric function

$Rb_3Sb_2Br_9$		$Rb_3Sb_2Br_6I_3$	
ν_{TO} (cm^{-1})	ν_{LO} (cm^{-1})	ν_{TO} (cm^{-1})	ν_{LO} (cm^{-1})
56	63	49	62
66	68		
81	86		
118	128	110	134
133	144		
151	160	157	171
182	192	181	209
196	223		

4. Discussion

4.1. Local octahedral distortion

The interatomic distances were analyzed and revealed that [SbX_6] octahedra have a non-negligible distortion in all the cases (symmetry, temperature, and iodine doping). In this distorted configuration, the Sb atom is displaced from the geometric center of the octahedron toward one of its faces, resulting in an asymmetric coordination environment, in which three halide ligands are significantly closer than the remaining three. Table 4 lists the main interatomic distances of Sb for both phases in the two observed symmetries. The average Sb–X distances for pristine and doped phases as a function of temperature in plotted in Fig. 9. In Table 4 and Fig. 9, the averages of the shortest and longest Sb–X distances are indicated by the letters S and L, respectively. This off-center displacement of Sb was previously reported for $Rb_3Sb_2Br_9$ and $Rb_3Sb_2I_9$ at room temperature.[46] In the present study, it is possible to notice that this behavior persists from 80 K up to the decomposition temperature. Furthermore, in the mixed-

Table 4 Main interatomic distances for $Rb_3Sb_2Br_9$ and $Rb_3Sb_2Br_6I_3$ halides for both monoclinic $P2_1/n$ (298 K) and trigonal $P\bar{3}m1$ (400 K)

Sb–X distances for monoclinic $P2_1/n$ (298 K)

$Rb_3Sb_2Br_9$			$Rb_3Sb_2Br_6I_3$		
Sb1–X	Sb1–Br	⟨Sb1–Br⟩		Sb1–Br/I	⟨Sb1–Br/I⟩
Br7	2.57(2)		Br7/I7	2.696(8)	
Br5	2.67(1)	2.65(2)^S	Br5/I3	2.739(8)	2.728(8)^S
Br3	2.72(1)		Br3/I3	2.749(6)	
Br1	2.89(2)		Br1	2.98(1)	
Br9	2.95(1)	2.93(2)^L	Br9	2.977(8)	2.99(1)^L
Br9	2.95(1)		Br9	3.025(8)	

Sb–X distances for monoclinic $P2_1/n$ (298 K)

$Rb_3Sb_2Br_9$			$Rb_3Sb_2Br_6I_3$		
Sb2–X	Sb2–Br	⟨Sb2–Br⟩		Sb2–Br/I	⟨Sb2–Br/I⟩
Br6	2.65(1)		Br6/I6	2.735(8)	
Br4	2.67(1)	2.67(1)^S	Br4/I4	2.756(8)	2.760(8)^S
Br2	2.68(1)		Br2/I2	2.789(8)	
Br8	2.88(1)		Br8	2.982(9)	
Br1	2.95(2)	2.94(2)^L	Br1	3.00(1)	3.00(1)^L
Br8	3.00(2)		Br8	3.027(8)	

Sb–X distances for trigonal $P\bar{3}m1$ (400 K)

$Rb_3Sb_2Br_9$		$Rb_3Sb_2Br_6I_3$	
	Sb–Br		Sb1–Br/I
Br2	2.612(1)^S	Br2/I2	2.713(3)^S
Br1	2.9160(8)^L	Br1/I1	2.966(2)^L

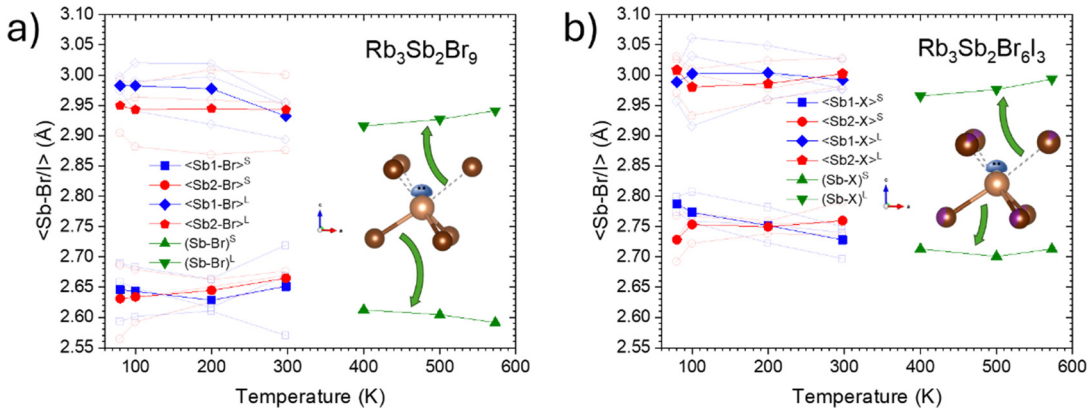

Fig. 9 Thermal evolution Sb–X (X = Br, I) bond distances for (a) $Rb_3Sb_2Br_9$ and (b) $Rb_3Sb_2Br_6I_3$. The angular bond distortions may suggest the occurrence of a stereochemical active lone pair on the Sb^{3+} atoms.

halide phase, where Sb is coordinated in an asymmetric environment [$Sb(Br_4I_2)$], it is notable that Sb preferentially bonds to the site occupied by Br and I in approximately equal proportions, rather than to the site predominantly occupied by Br. In this quasi-pyramidal geometry, the X–Sb–X angles are 92.60(5)° and 93.1(1)° for pristine and doped phases, respectively. These values are slightly above 90°, expected for an undistorted octahedron, and significantly lower than those typical of a sp^3 hybridized environment. Therefore, the observed angular bond distortion plausibly suggests the presence of a stereochemical active lone pair on the Sb^{3+} atoms.

4.2. Distortion-mode analysis

The structural differences between monoclinic and trigonal phases can be visualized as structural distortions acting on the trigonal phase. The low-symmetry distorted unit-cell can be represented as a linear combination of 'frozen' distortion-modes, each transforming according to a specific irreducible representation (irrep) of the high-symmetry space-group.[31] Initially, one needs to express the atomic positions of the low-symmetry phase ($\boldsymbol{r}$; subgroup H) in terms of those of the high-symmetry structure ($\boldsymbol{r}_0$; supergroup G), with the latter transformed into the unit-cell basis of the subgroup H. This relationship can be written as follows:

$$\boldsymbol{u}(\mu,i) = \boldsymbol{r}(\mu,i) - \boldsymbol{r}_0(\mu,i) = \sum_{(\tau,m)} A_{(\tau,m)}\hat{\boldsymbol{e}}_{(\tau,m)}(\mu,i) \qquad (1)$$

μ denotes the distinct atomic species (or crystallographic sites) in the asymmetric unit, and $i = 1\ldots n_\mu$ indexes the atoms associated with each site. The displacement vectors $\boldsymbol{u}(\mu,i)$ are linearly decomposed onto the basis vectors of the irreducible representations (irreps) obtained from the group–subgroup analysis.[31] In this notation, $\hat{\boldsymbol{e}}_{(\tau,m)}(\mu,i)$ denotes the polarization (basis) vector of the irrep (τ), while m indexes the independent modes associated with that irrep (τ), and $A_{(\tau,m)}$ is the corresponding distortion amplitude.

This distortion-mode analysis was employed to find the respective amplitudes and polarization vectors of the symmetry-adapted distortion modes, principally to shed light into the driven mechanism of trigonal ↔ monoclinic transition in $Rb_3Sb_2Br_9$ halide. As a starting point, we employed the monoclinic structure of $Rb_3Sb_2Br_9$ refined at 80 K (subgroup H) together with its trigonal phase refined at 500 K (supergroup G). These crystallographic models were used as input for the Amplimodes algorithm,[31–33] available on the Bilbao Crystallographic Server.[41] Within this framework, the structural distortion is rigorously decomposed according to eqn (1), enabling a detailed symmetry-mode analysis of the transition. Prior to this step, the monoclinic structure was transformed into its standard setting ($P2_1/c$) using the CIF2Standard tool[41] to ensure consistency between subgroup and supergroup descriptions (see Table S7). Crystallographic data of the trigonal phase at 500 K are listed in Table S8. The transformation matrix (P,p) relating both unit cells is also provided in the SI. The irreducible representations are labeled using the k-vector notation in the first Brillouin zone (Γ, A, L, and M). The decomposition of the low-symmetry monoclinic phase in terms of the irreps of the trigonal high-symmetry leads to the site splitting resumed in Table 5. The corresponding symmetry-adapted mode amplitudes are listed in Table 5. This site splitting provides a systematic basis for identifying the number, symmetry, and physical character of the distortion modes that stabilize the low-symmetry phase.

From the site splitting analysis summarized in Table 5, a total of forty-two symmetry-adapted ('frozen') distortion modes are required to properly describe the monoclinic distortion of $Rb_3Sb_2Br_9$ with respect to its trigonal parent structure. These modes are distributed among six irreducible representations (Γ_1^+, Γ_3^+, A_1^-, A_3^-, L_2^-, and M_2^+). At the Rb1 site (1a) of the trigonal phase, the splitting into the monoclinic 4e position activates three modes [$A_3^-(1) + L_2^-(2)$]. The Rb2 sites (2d) split into two independent positions (Rb2 and Rb3), giving rise to six distortion-modes [$\Gamma_1^+(1) + \Gamma_3^+(1) + A_3^-(1) + L_2^-(2) + M_2^+(1)$]. A similar situation occurs at the Sb1 sites (2d), where the splitting into Sb1 and Sb2 generates six modes of identical symmetry modes [$\Gamma_1^+(1) + \Gamma_3^+(1) + A_3^-(1) + L_2^-(2) + M_2^+(1)$]. For the Br1 sites (3e), the splitting into three positions (Br1, Br2, and Br3) produces nine distortion-modes [$A_1^-(1) + A_3^-(3) + L_2^-(2) + M_2^+(3)$]. Finally, the Br2

Table 5 Symmetry mode analysis of the $Rb_3Sb_2Br_9$ structure elucidating the site splitting for the low symmetry phase ($P2_1/c$ at 80 K) and the symmetry-adapted modes responsible for the symmetry lowering from the trigonal phase ($P\bar{3}m1$ at 500 K). The corresponding amplitudes of the symmetry-adapted modes (normalized within the primitive unit-cell of the high-symmetry structure) are also listed

$P\bar{3}m1$ (#164)	$P2_1/c$ (#14)	Symmetry-adapted modes for each Wyckoff site
Rb1 (1a)	Rb1 (4e)	$A_3^-(1) + L_2^-(2)$
Rb2 (2d)	Rb2–3 (4e)	$\Gamma_1^+(1) + \Gamma_3^+(1) + A_3^-(1) + L_2^-(2) + M_2^+(1)$
Sb1 (2d)	Sb1–2 (4e)	$\Gamma_1^+(1) + \Gamma_3^+(1) + A_3^-(1) + L_2^-(2) + M_2^+(1)$
Br1 (3e)	Br1–3 (4e)	$A_1^-(1) + A_3^-(3) + L_2^-(2) + M_2^+(3)$
Br2 (6i)	Br4–9 (4e)	$\Gamma_1^+(2) + \Gamma_3^+(3) + A_1^-(1) + A_3^-(3) + L_2^-(5) + M_2^+(4)$

Irreps	Γ_1^+	Γ_3^+	A_1^-	A_3^-	L_2^-	M_2^+
Direction	(a)	$\left(-\frac{1}{2}a, \frac{\sqrt{3}}{2}a\right)$	(a)	$\left(-\frac{1}{2}a, \frac{\sqrt{3}}{2}a\right)$	$(0\ a\ 0)$	$(0\ a\ 0)$
Dimension	4	5	2	9	13	9
Amplitude (Å)	0.1404	0.1718	0.9904	0.6761	0.7711	1.2803
k-vector	(0,0,0)	(0,0,0)	$\left(0,0,\frac{1}{2}\right)$	$\left(0,0,\frac{1}{2}\right)$	$\left(\frac{1}{2},0,\frac{1}{2}\right)$	$\left(\frac{1}{2},0,0\right)$
Isotropy group	$P\bar{3}m1$	$C2/m$	$P\bar{3}c1$	$C2/c$	$C2/m$	$P2_1/c$

sites (6i) split into six distinct positions (Br4–Br9), which contribute the largest number of modes, namely eighteen $[\Gamma_1^+(2) + \Gamma_3^+(3) + A_1^-(1) + A_3^-(3) + L_2^-(5) + M_2^+(4)]$. Collectively, these distortions define the complete set of symmetry-adapted modes responsible for the monoclinic distortion of $Rb_3Sb_2Br_9$.

From the symmetry-mode amplitudes resumed in Table 5, it is clear that the monoclinic distortion in $Rb_3Sb_2Br_9$ is dominated by the M_2^+ (amplitude of ~1.28 Å), A_1^- (amplitude of ~0.99 Å), and A_3^- (amplitude of ~0.68 Å) modes, which correspond to in-phase and out-of-phase rotations of $[Sb1Br_6]$ and $[Sb2Br_6]$ octahedra, as illustrated by the polarization vectors in Fig. 10 and Fig. S5 [where alternative structural views focusing exclusively on the Sb1 and Sb2 octahedra are shown for clarity]. In contrast, the Γ_1^+ and Γ_3^+ modes, associated with symmetric and anti-symmetric octahedral stretching, show much smaller distortion amplitudes (~0.14 and ~0.17 Å,

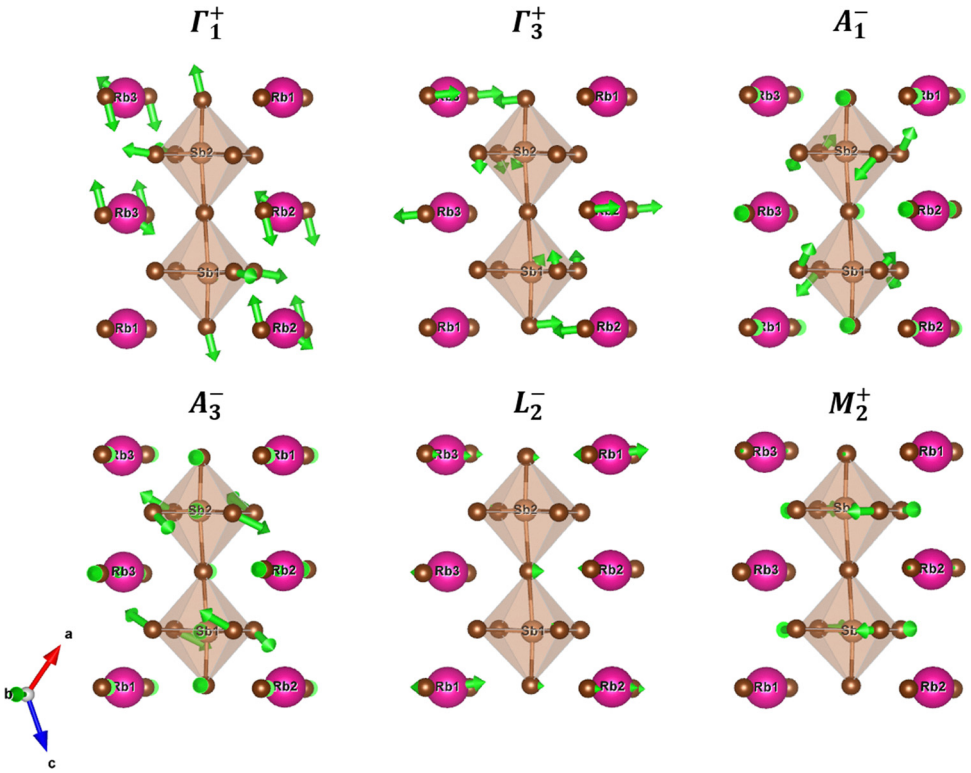

Fig. 10 The structural diagrams illustrate the atomic movements (polarization vectors) for symmetry-adapted modes during a change in symmetry from trigonal to monoclinic in $Rb_3Sb_2Br_9$ halide. The green arrows represent the magnitude and direction of these distortions, as determined by the Amplimodes algorithm.[31–33] Brown spheres represent the bromide atoms.

respectively) and thus contribute only marginally to monoclinic distortion. The L_2^- mode corresponds to rigid translations of Rb cations and exhibits intermediate amplitude ($\sim$0.77 Å), making a moderate contribution to the overall distortion. Altogether, these results indicate that the symmetry lowering from trigonal to monoclinic is primarily driven by cooperative octahedral rotations, while bond-length changes and cation translations act as secondary distortions that fine-tune the stability of the low-symmetry phase. According to Landau's theory of phase transitions,[33,47] the primary order parameter drives the symmetry change, while secondary modes are induced by the primary distortion. In the monoclinic-to-trigonal transition, the octahedral tilting mode acts as the primary mode, whereas all other distortion modes develop as secondary responses. This classification allows a clear understanding of the symmetry-breaking mechanism and the contributions of individual distortion modes to the structural transition.

5. Conclusions

In short, we demonstrate that mechanochemistry enables the scalable, green synthesis of $Rb_3Sb_2Br_9$ and $Rb_3Sb_2Br_6I_3$ halides, which exhibit rich polymorphism and tunable optoelectronic properties. High-resolution synchrotron X-ray diffraction combined with symmetry-adapted distortion-mode analysis reveals that the trigonal to monoclinic transition is governed primarily by cooperative [SbX_6] (X = Br, I) octahedral rotations and Sb^{3+} lone-pair activity, while Rb^+ displacements and bond deformations provide secondary stabilization. This structural hierarchy explains the persistence of distortions across a wide temperature range and clarifies the link between local coordination asymmetry and electronic gap tuning. The infrared response confirms fewer resolved phonon modes than group theory predicts, with red shifts and broadening in the iodide-rich phase pointing to local I^- ordering and higher structural disorder. The optical band gap of the monoclinic specimens for $Rb_3Sb_2Br_9$ and $Rb_3Sb_2Br_6I_3$ are $\sim$2.87 eV and $\sim$2.52 eV, respectively. The resulting band gaps place these phases in the visible range, underscoring their promise for lead-free and tunable optoelectronic applications. More broadly, our findings demonstrate how mechanochemistry synthesis and mode-resolved crystallography can be combined to uncover hidden structure–property relationships in halide perovskite derivatives, paving the way for the rational design of stable, non-toxic materials for solar energy and beyond.

Author contributions

Y. Chakroun, W. Cherif, J. Gainza, R. Silva, and F. Serrano contributed to methodology. Y. Chakroun, B. Martinelli, M. M. Ferrer, and C. Pecharromán performed investigation, formal analysis, and provided resources. C. A. López, J. E. F. S. Rodrigues, and J. A. Alonso contributed to conceptualization, methodology, investigation, formal analysis, visualization, and writing; J. E. F. S. Rodrigues and J. A. Alonso also supervised the work, and J. A. Alonso acquired funding. All authors discussed the results and approved the final manuscript.

Conflicts of interest

There are no conflicts to declare.

Data availability

Synchrotron X-ray diffraction data described in this article are available at the European Synchrotron Radiation Facility (ESRF) repository, for experiment HC5818.[48]

Supplementary information (SI): Differential scanning calorimetry (DSC) and thermogravimetric (TG) analysis for $Rb_3Sb_2Br_9$ and $Rb_3Sb_2Br_6I_3$. SEM and EDXS spectra. Structural data from SXRD for the trigonal phase. Raw far- and mid-infrared spectra of $Rb_3Sb_2Br_9$ and $Rb_3Sb_2Br_6I_3$. Further details on the distortion-mode analysis in $Rb_3Sb_2Br_9$. See DOI: **https://doi.org/10.1039/d5tc03197d**.

Acknowledgements

All the authors acknowledge financial support of the Spanish Ministry for Science and Innovation [MCIN/AEI/10.13039/501100011033] with grant numbers: PID2021-122477OB-I00 and TED2021-129254B-C22. CAL is grateful to UNSL and ANPCyT for the financial support [grant number: PROICO 2-2320 and PICT2020A-2437], in Argentine. This work was also supported by Fundação de Amparo à Pesquisa do Estado do Rio Grande do Sul [FAPERGS, Grant 23/2551-0000153-5], Conselho Nacional de Desenvolvimento Científico e Tecnológico [CNPq, Grants 406160/2023-6, 307213/2021-8, 150187/2023-8, and 314278/2023-0], and Fundação de Amparo à Pesquisa do Estado de São Paulo [FAPESP, Grants 22/03959-6, 22/16509-9, and 20/01144-0]. The authors thank the staff of the European Synchrotron Radiation Facility (ESRF) for technical assistance during synchrotron X-ray powder diffraction experiments (experiment: HC-5818[48]).

References

1 A. K. Jena, A. Kulkarni and T. Miyasaka, *Chem. Rev.*, 2019, **119**, 3036–3103.
2 M. V. Kovalenko, L. Protesescu and M. I. Bodnarchuk, *Science*, 2017, **358**, 745–750.
3 N.-G. Park, M. Grätzel, T. Miyasaka, K. Zhu and K. Emery, *Nat. Energy*, 2016, **1**, 16152.
4 A. M. A. Leguy, Y. Hu, M. Campoy-Quiles, M. I. Alonso, O. J. Weber, P. Azarhoosh, M. van Schilfgaarde, M. T. Weller, T. Bein, J. Nelson, P. Docampo and P. R. F. Barnes, *Chem. Mater.*, 2015, **27**, 3397–3407.
5 J. Xiong, N. Liu, X. Hu, Y. Qi, W. Liu, J. Dai, Y. Zhang, Z. Dai, X. Zhang, Y. Huang, Z. Zhang, Q. Dai and J. Zhang, *Adv. Energy Mater.*, 2022, **12**, 2201787.

6 C. Li, F. Xu, Y. Li, N. Li, H. Yu, B. Yuanb, Z. Chen, L. Li and B. Cao, *Sol. Energy*, 2022, **233**, 271–277.
7 S. Chen, X. Zhang, J. Zhao, Y. Zhang, G. Kong, Q. Li, N. Li, Y. Yu, N. Xu, J. Zhang, K. Liu, Q. Zhao, J. Cao, J. Feng, X. Li, J. Qi, D. Yu, J. Li and P. Gao, *Nat. Commun.*, 2018, **9**, 4807.
8 W. Ming, D. Yang, T. Li, L. Zhang and M. Du, *Adv. Sci.*, 2018, **5**, 1700662.
9 Y. Chen, Z. Yue, S.-W. Tsang and Y. Cheng, *Nano Energy*, 2025, **137**, 110782.
10 G. Yang, H. Gu, J. Yin, C. Fei, Z. Shi, X. Shi, X. Ying and J. Huang, *Nat. Sustainability*, 2025, **8**, 456–463.
11 N. K. Noel, S. D. Stranks, A. Abate, C. Wehrenfennig, S. Guarnera, A.-A. Haghighirad, A. Sadhanala, G. E. Eperon, S. K. Pathak, M. B. Johnston, A. Petrozza, L. M. Herz and H. J. Snaith, *Energy Environ. Sci.*, 2014, **7**, 3061–3068.
12 F. Hao, C. C. Stoumpos, D. H. Cao, R. P. H. Chang and M. G. Kanatzidis, *Nat. Photonics*, 2014, **8**, 489–494.
13 Z. Shi, J. Guo, Y. Chen, Q. Li, Y. Pan, H. Zhang, Y. Xia and W. Huang, *Adv. Mater.*, 2017, **29**, 1605005.
14 S. Lu, Q. Zhou, Y. Ouyang, Y. Guo, Q. Li and J. Wang, *Nat. Commun.*, 2018, **9**, 3405.
15 K. Ahmad and S. M. Mobin, *ACS Omega*, 2020, **5**, 28404–28412.
16 S. Weber, T. Rath, K. Fellner, R. Fischer, R. Resel, B. Kunert, T. Dimopoulos, A. Steinegger and G. Trimmel, *ACS Appl. Energy Mater.*, 2019, **2**, 539–547.
17 M. Y. Valakh, M. P. Lisitsa, E. Y. Peresh, O. V. Trylis and A. M. Yaremko, *J. Mol. Struct.*, 1997, **436–437**, 309–313.
18 C. C. Byeon, *New Phys.: Sae Mulli*, 2019, **69**, 149–153.
19 J. P. Correa-Baena, A. Abate, M. Saliba, W. Tress, T. Jesper Jacobsson, M. Grätzel and A. Hagfeldt, *Energy Environ. Sci.*, 2017, **10**, 710–727.
20 D. P. McMeekin, G. Sadoughi, W. Rehman, G. E. Eperon, M. Saliba, M. T. Hörantner, A. Haghighirad, N. Sakai, L. Korte, B. Rech, M. B. Johnston, L. M. Herz and H. J. Snaith, *Science*, 2016, **351**, 151–155.
21 C. A. López, C. Abia, J. Gainza, J. E. Rodrigues, B. Martinelli, F. Serrano-Sánchez, R. S. Silva, M. M. Ferrer, O. J. Dura, J. L. Martínez, M. T. Fernández-Díaz and J. A. Alonso, *Inorg. Chem.*, 2024, **63**, 12641–12650.
22 C. Abia, C. A. López, J. Gainza, J. E. F. S. S. Rodrigues, B. Fragoso, M. M. Ferrer, N. M. Nemes, O. J. Dura, J. L. Martínez, M. T. Fernández-Díaz and J. A. Alonso, *CrystEngComm*, 2023, **25**, 1857–1868.
23 C. Abia, C. A. López, J. Gainza, J. E. F. S. Rodrigues, B. Fragoso, M. M. Ferrer, M. T. Fernández-Díaz, F. Fauth, J. L. Martínez and J. A. Alonso, *ACS Appl. Mater. Interfaces*, 2023, **15**, 40762–40771.
24 C. Abia, C. A. López, J. Gainza, J. E. F. S. Rodrigues, M. M. Ferrer, N. M. Nemes, O. J. Dura, J. L. Martínez, M. T. Fernández-Díaz, C. Álvarez-Galván, G. Németh, K. Kamarás, F. Fauth and J. A. Alonso, *J. Mater. Chem. C*, 2022, **10**, 6857–6865.
25 C. Abia, C. A. López, J. Gainza, J. E. F. S. Rodrigues, M. M. Ferrer, G. Dalenogare, N. M. Nemes, O. J. Dura, J. L. Martínez, M. T. Fernández-Díaz, C. Álvarez-Galván and J. A. Alonso, *Inorg. Chem.*, 2022, **61**, 5502–5511.
26 Y. Chakroun, W. Cherif, F. S. M. Rodrigues, L. Ktari, C. A. López, F. Serrano-Sánchez, F. G. Alabarse, M. M. Ferrer, J. E. F. S. Rodrigues and J. A. Alonso, *Inorg. Chem.*, 2024, **63**, 22258–22272.
27 K. M. McCall, C. C. Stoumpos, S. S. Kostina, M. G. Kanatzidis and B. W. Wessels, *Chem. Mater.*, 2017, **29**, 4129–4145.
28 K. M. McCall, Z. Liu, G. Trimarchi, C. C. Stoumpos, W. Lin, Y. He, I. Hadar, M. G. Kanatzidis and B. W. Wessels, *ACS Photonics*, 2018, **5**, 3748–3762.
29 J. P. Correa-Baena, L. Nienhaus, R. C. Kurchin, S. S. Shin, S. Wieghold, N. T. Putri Hartono, M. Layurova, N. D. Klein, J. R. Poindexter, A. Polizzotti, S. Sun, M. G. Bawendi and T. Buonassisi, *Chem. Mater.*, 2018, **30**, 3734–3742.
30 Q. Luo, D. Xie, Y. Tian, C. Zhang, D. Cao, X. Chen, P. Liang and H. Shu, *J. Mater. Chem. C*, 2024, **12**, 13061–13072.
31 J. M. Perez-Mato, D. Orobengoa and M. I. Aroyo, Mode crystallography of distorted structures, *Acta Crystallogr., Sect. A: Found. Crystallogr.*, 2010, **66**, 558–590.
32 M. I. Aroyo, J. M. Perez-Mato, C. Capillas, E. Kroumova, S. Ivantchev, G. Madariaga, A. Kirov and H. Wondratschek, *Z. Kristallogr. - Cryst. Mater.*, 2006, **221**, 15–27.
33 J. M. Perez-Mato, D. Orobengoa, M. I. Aroyo and L. Elcoro, *J. Phys.: Conf. Ser.*, 2010, **226**, 012011.
34 A. Fitch, C. Dejoie, E. Covacci, G. Confalonieri, O. Grendal, L. Claustre, P. Guillou, J. Kieffer, W. de Nolf, S. Petitdemange, M. Ruat and Y. Watier, *J. Synchrotron Radiat.*, 2023, **30**, 1–10.
35 J. Rodríguez-Carvajal, *Phys. B*, 1993, **192**, 55–69.
36 A. Erba, J. K. Desmarais, S. Casassa, B. Civalleri, L. Donà, I. J. Bush, B. Searle, L. Maschio, L. Edith-Daga, A. Cossard, C. Ribaldone, E. Ascrizzi, N. L. Marana, J.-P. Flament and B. Kirtman, *J. Chem. Theory Comput.*, 2023, **19**, 6891–6932.
37 J. P. Perdew, A. Ruzsinszky, G. I. Csonka, O. A. Vydrov, G. E. Scuseria, L. A. Constantin, X. Zhou and K. Burke, *Phys. Rev. Lett.*, 2008, **100**, 136406.
38 J. Laun, D. Vilela Oliveira and T. Bredow, *J. Comput. Chem.*, 2018, **39**, 1285–1290.
39 I. Abrahams, D. Z. Demetriou, R. T. Kroemer, H. Taylor and M. Motevalli, *J. Solid State Chem.*, 2001, **160**, 382–387.
40 E. Y. Peresh, V. I. Sidei, O. V. Zubaka and I. P. Stercho, *Inorg. Mater.*, 2011, **47**, 208–212.
41 E. Kroumova, M. I. Aroyo, J. M. Perez-Mato, A. Kirov, C. Capillas, S. Ivantchev and H. Wondratschek, *Phase Transitions*, 2003, **76**, 155–170.
42 D. L. Rousseau, R. P. Bauman and S. P. S. Porto, *J. Raman Spectrosc.*, 1981, **10**, 253–290.
43 J. E. F. S. Rodrigues, M. M. Ferrer, M. L. Moreira, J. R. Sambrano, R. C. Costa, A. D. Rodrigues, P. S. Pizani, Y. Huttel, J. A. Alonso and C. Pecharromán, *J. Alloys Compd.*, 2020, **813**, 152136.

44 C. Pecharromán and J. E. Iglesias, *Appl. Spectrosc.*, 2000, **54**, 634–638.
45 J. E. F. S. Rodrigues, C. A. Escanhoela, B. Fragoso, G. Sombrio, M. M. Ferrer, C. Álvarez-Galván, M. T. Fernández-Díaz, J. A. Souza, F. F. Ferreira, C. Pecharromán and J. A. Alonso, *Ind. Eng. Chem. Res.*, 2021, **60**, 18918–18928.
46 J. Chang, T. Doert and M. Ruck, *Z. Anorg. Allg. Chem.*, 2016, **642**, 736–748.
47 L. D. Landau and E. M. Lifshitz, *Statistical Physics: Volume 5, Part 1*, Pergamon, Oxford, 1st edn, 1959.
48 J. A. Alonso, M. Chivite Lacaba, J. E. Figueiredo Soares Rodrigues, J. Gainza Martin and R. Santos Silva Jr., Unveiling the structure and lone pair behaviour of the Pb-free halides A3Bi2Br9 and A3Bi2Br6I3 (A = Cs, Rb), with photovoltaic applications [Dataset], European Synchrotron Radiation Facility, 2027, DOI: 10.15151/ESRF-ES-1911533009.